**Proceedings of the Canadian Society for Mechanical Engineering International Congress**
**32nd Annual Conference of the Computational Fluid Dynamics Society of Canada**
**Canadian Society of Rheology Symposium**
**CSME-CFDSC-CSR 2025**
**May 25–28, 2025, Montréal, Québec, Canada**

# Shape Optimization of a Quiet and Efficient Synthetic Jet Actuator Enclosure using COMSOL Multiphysics

Trish A. Maduche[1], Luc G. Mongeau[1], Amanda Kronish[1], Christopher Morales[1]
[1] Department of Mechanical Engineering, McGill University
Montreal, Canada

***Abstract***—A streamlined enclosure was designed for an actuator to be used as a surface-cleaning device. The main goal was to produce a compact, aerodynamic-efficient enclosure that enhances the intrinsic dipole cancellations between the sound emissions of two orifices, the actuator orifice and the enclosure orifice, with minimal impact on cleaning performance. To improve the aerodynamic efficiency of the enclosure, several steps were taken towards producing an optimized enclosure shape. A preliminary parametric study was conducted on three enclosure designs to determine the best initial design. Geometric and shape optimization were performed with the objective of minimizing the pressure drop, which maximizes the enclosure's aerodynamic efficiency. Factors such as mesh construction and adaptive mesh refinement, numerical turbulence models, optimization algorithms, and the maximum displacement setting were explored in COMSOL Multiphysics to converge to the optimum enclosure design.

***Keywords – Synthetic jet actuator, COMSOL Multiphysics, optimization, adaptive mesh refinement***

## I. INTRODUCTION

Synthetic jet actuators (SJAs) are devices that generate a pulsatile flow through cyclic suction and discharge while maintaining a zero net mass flux [1]. Their distinct ability to operate with no external fluid source, short response time, and compactness [1] make them suitable for use in flow control in aircraft, thrust vectoring in jet engines, and sensor cleaning in automobiles. Due to their potential use in engineering systems, it is important to investigate and improve their performance.

Most synthetic jet actuators consist of an actuator, a cavity, and an orifice or jet slot [1]. A typical actuator is integrated within at least one of the walls of the cavity [2], as shown in Figure.1. The actuator, usually a mechanical piston, oscillating diaphragm, or loudspeaker, is movable to supply the cyclic fluid suction and discharge into the cavity to produce the synthetic jets [1, 3]. A standard synthetic jet actuator comprises a vibrating diaphragm(s), a cylindrical cavity, and an orifice [1]. The pulsatile movement of the vibrating diaphragm causes fluid displacement in the cavity and generates the synthetic jets.

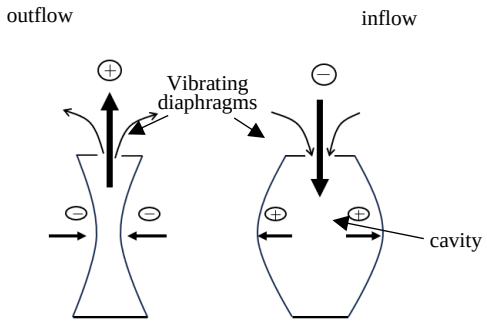


Figure 1. Schematic of a standard synthetic jet actuator with two diaphragms

This study aims to test the hypothesis that a streamlined enclosure improves the overall performance of a synthetic jet actuator. The main objectives are to (i) design a streamlined enclosure for a synthetic jet actuator and (ii) perform an optimization study in COMSOL Multiphysics to determine the profile that minimizes energy losses inside the enclosure towards the goal of improving the overall efficiency of the enclosure.

## II. LITERATURE REVIEW

Synthetic jet actuators' performance is potentially useful in different sectors. In electronics cooling, SJAs are a promising alternative to fan-driven cooling systems and heat sinks due to their ability to generate turbulence through the cyclic suction and expulsion of fluid [4]. Their potential use in active flow control to reduce drag, abate flow separation [5], and reduce power consumption has been studied [6]. Experimental and computational analysis has been performed to further understand synthetic jet actuators' performance and the noise produced as an unwanted by-product. One way to analyze the performance is through geometric parameter analysis of the actuator's aspect ratio and orifice and cavity shape and size [4]. Noise reduction techniques that other researchers have explored

Natural Sciences and Engineering Research Council of Canada (NSERC) and McCall MacBain Scholarships at McGill *(sponsors)*

include feedforward harmonic suppression [7] and double chamber actuators with lobbed orifices [8].

Reference [3] explored different noise abatement techniques for synthetic jet actuators to increase their application in systems that require low noise levels. One technique was the use of a cubic enclosure and a muffler. The results showed a reduction in the sound produced, but the enclosure implementation was impractical due to its size.

Reference [9] investigated the two main sources of sound, the structure-borne and air-borne sound, as monopoles. To isolate the structure-borne component of the noise produced by the actuator, an enclosure with sound-absorbing foam was used to enclose the actuator's diaphragm. The results showed decreased jet velocity and increased sound pressure levels. The conclusion on the increase in sound was that the actuator with no enclosure had an intrinsic noise cancellation between the two monopoles, compared to the diaphragm-enclosed actuator that had only one monopole: the air-borne sound.

This project proposes modifying the enclosure by (i) streamlining it and (ii) adding a secondary orifice that enhances the intrinsic dipole cancellations between the sound emissions of two orifices: the actuator orifice and the enclosure orifice.

## III. METHODOLOGY

The correct adjustment of optimization processes leads to convergence to a true, optimal result [10]. Figure 2 details the processes followed, from modelling the three proposed enclosure designs to obtaining the optimum enclosure shape used to design the 3-D enclosure.

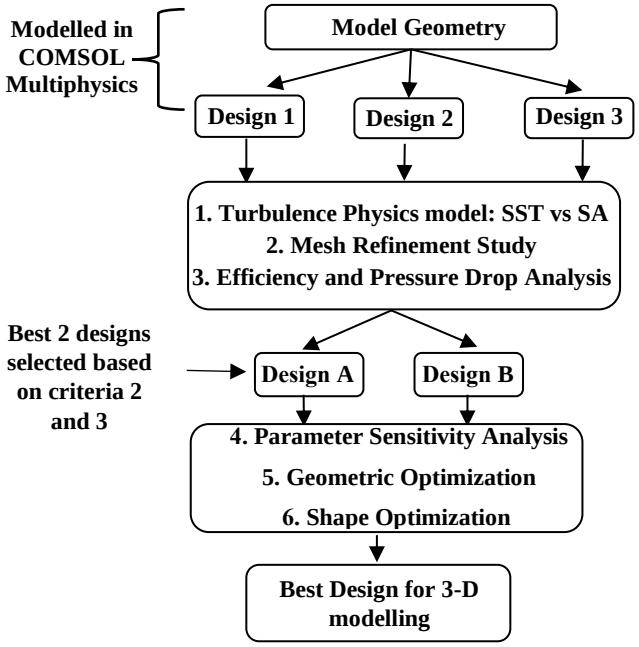


Figure 2. Flow chart of the procedure for optimization.

Three enclosure designs were modelled in COMSOL Multiphysics, and the dimensions were based on a 102.5 mm long, aluminum, piezoelectric synthetic jet actuator (Figure 3) available for experimental work. The 2D designs (Figure 4) are a side view of the assembled enclosure and actuator. The enclosure designs' shapes differed in their apex positions on the x-axis.

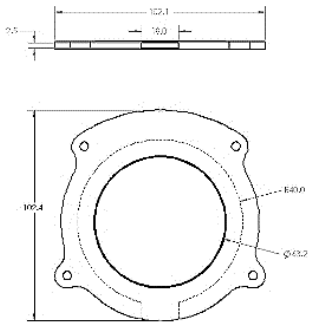

Figure 3. Schematic of the piezoelectric SJA for experimental testing.

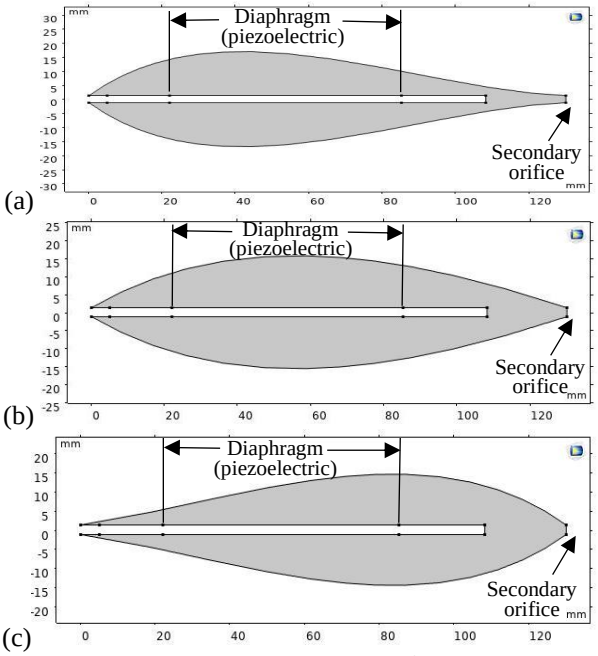


Figure 4. (a) Design 1 (b) Design 2 (c) Design 3 of the enclosure modelled in COMSOL Multiphysics.

The inlet is the piezoelectric diaphragm, and the outlet is the enclosure's secondary orifice.

### A. *Turbulence Physics Models*

Turbulence modelling is one of three fundamental elements of CFD [11], the other two being grid generation and algorithm development. An ideal turbulence model has minimum complexity but higher accuracy, meaning it approximates the physical flow behaviour with higher precision [11].

The convergence and performance of turbulence numerical models were investigated for two turbulence physics models: (i) a one-equation numerical model, Turbulence Spalart-Allmaras [11, 12], and (ii) a two-equations model, Menter's Shear Stress Transport turbulence (SST) [13]. The two physics models were compared using computational time. The pressure at the enclosure orifice (outlet pressure), velocity magnitude, and total viscous dissipation from both models were compared.

*Boundary Conditions*

A **velocity inlet** boundary condition with a peak amplitude of 0.4 m/s at the center of the cavity was set on the diaphragm. A **pressure boundary** condition of 0 Pa static pressure was applied at the outlet to ensure that the outflow pressure was equal to the atmospheric pressure. A no-slip boundary condition was applied to the walls.

*B. Mesh Refinement Study*

Meshing is one of the most important aspects of finite element analysis because it directly influences convergence, stability, and accuracy [14]. A selected mesh should be able to fully capture the fluid flow structure. For flows with vortices or recirculation, the fluid needs to be refined or clustered in the wall boundaries [14]. In this study, where recirculation and flow separation are expected, a mesh sensitivity analysis was conducted to determine a well-structured mesh that produces accurate results. Five of the nine physics-controlled mesh sizes in COMSOL Multiphysics were generated, and the mesh quality was analyzed based on the mesh skewness.

*Adaptive Mesh Refinement*

Adaptive Mesh Refinement involves refining the mesh or clustering grid points in areas of complex flow or large flow gradients while decluttering grid points in areas where finer meshes are redundant [14]. Figure 5 illustrates Design 3 with (a) a physics-controlled 'extremely fine' mesh and (b) an example of one of the meshes generated from the Adaptive Mesh Refinement.

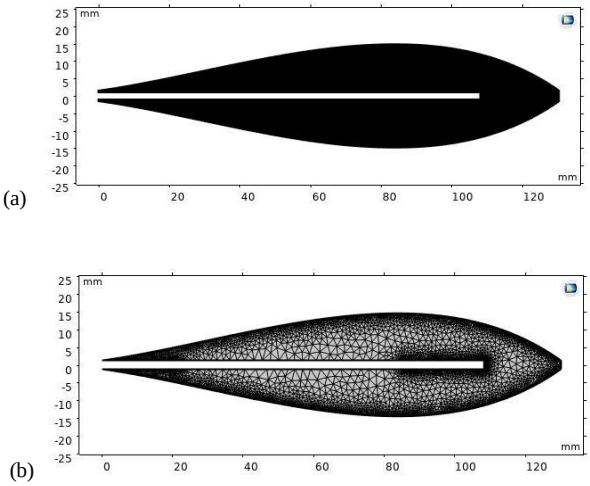


Figure 5. (a) a physics-controlled mesh and (b) one of the meshes generated through Adaptive Mesh Refinement.

The effect of mesh size and quality on computational time and accuracy was investigated alongside the study of the most suitable turbulence model.

*Enclosure Efficiency and Pressure Drop*

The efficiency of internal viscous flows is attributed to the minimization of head losses in the control volume. Pressure losses form a component of major losses in head loss. In viscous fluid flow, the nature of pressure losses is determined using the energy equation [15]

$$\dot{Q} - \dot{W} = \frac{\partial}{\partial t}\int_{CV} e\,\partial\forall + \int_{CS}(e + Pv)\rho\vec{V}\,d\vec{A}, \quad (1)$$

Where energy per unit mass, $e, = u + \frac{V^2}{2} + gz$ and v is the specific volume, equivalent to $\frac{1}{\rho}$ in incompressible flow [16]. $\dot{Q}$ is the rate of heat transferred to the system, and $\dot{W}$ is the rate of work done by the system [16]. P and V are the pressure and velocity at each point on the cross-section, respectively. $\vec{V}$ is the average velocity, A is the area, ρ is the density, g is the acceleration due to gravity, and z is the elevation. CV is the control volume, and CS is the control surface. Under steady-state conditions ($\frac{\partial}{\partial t} = 0$), assuming $\dot{W} = 0$, and in horizontal flow ($\Delta z = 0$), the equation reduces to

$$\dot{Q} = \int_{CS}\left(u_{in} + \frac{P_{in}}{\rho} + \frac{V_{in}^2}{2}\right)\rho\overrightarrow{V_{in}}\,d\overrightarrow{A_{in}} - \int_{CS}\left(u_{out} + \frac{P_{out}}{\rho} + \frac{V_{out}^2}{2}\right)\rho\overrightarrow{V_{out}}\,d\overrightarrow{A_{out}}. \quad (2)$$

In viscous flow, velocity *V* at a cross-section is not uniform; thus, integration is needed [15]. The term $\int_{CS}\left(\frac{P}{\rho} + \frac{V^2}{2}\right)\rho\vec{V}\,d\vec{A}$ represents the rate of change of mechanical energy at a cross-section. Assuming uniform internal energy, *u*, per cross-section, $\Delta u$ and $\dot{Q}$ present the rate of total energy loss in the system. The rate of change of internal energy at the inlet and outlet is used to calculate the efficiency of each enclosure design. In this study, the inlet velocity does not significantly change considering its constant supply on the piezoelectric diaphragm; hence, the rate of energy loss (power loss) can be majorly attributed to the pressure drop $\Delta P = P_1 - P_2$. The lower the pressure drop, the lower the power loss, and the greater the enclosure efficiency.

*C. Parameter Sensitivity Analysis*

A parametric sweep was performed on the length of the enclosure through a horizontal stretch factor *k* to investigate how its changes affect the enclosure's aerodynamic performance based on the specified parameter value list. The stretch factor *k* = $\frac{1}{b}$, where *b* is the actual stretch factor with values $0 < b < 1$. The enclosure's coordinates were transformed to (*k*x, y).

*D. Geometric Optimization*

The optimization was performed to determine the optimal enclosure length using three gradient-free algorithms in COMSOL Multiphysics: Nelder-Mead, BOBYQA (Bound Optimization BY Quadratic Approximation), and COBYLA (Constrained Optimization BY Linear Approximations) [17]. The objective function used is

$$\text{minimize } \Delta P = P_{in} - P_{out}$$
$$\text{subject to } -1.5\text{ Pa} \le P_{out} \le 1.5\text{ Pa}. \quad (3)$$

The constraint is a residual pressure allowance at the secondary orifice of the enclosure. The control variable is the horizontal stretch factor *k*, with a lower bound of 1 and an upper bound of 1.2. This means the enclosure length $L_{encl}$ was set to $130\text{mm} \le L_{encl} \le 156$ mm (Figure 6).

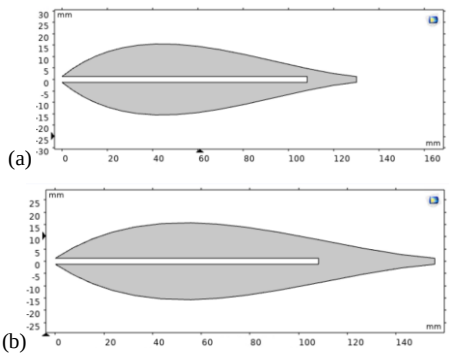


Figure 6. Variation in enclosure length from (a) 130mm to (b) 156mm.

### *E. Shape Optimization*

After the geometric optimization, gradient-based methods were used in shape optimization to determine the best shape of the enclosure polynomial boundary. The optimization algorithms used were the Sparse Nonlinear OPTimizer (SNOPT) and the Interior Point OPTimizer (IPOPT)[18]. The objective function and constraint were the same as those in the gradient-free optimization process. The optimality tolerance was set to 0.01, and the maximum number of iterations was set to 100.

#### *Maximum Displacement Setting $d_{max}$*

The maximum displacement setting in COMSOL Multiphysics is used to set the maximum allowable deviation of the geometry during optimization [10]. Research studies found on the effects of $d_{max}$ focused on structural shape optimization of shells [10]. Shape optimization works by deforming the mesh, thus decreasing mesh quality [17]. Therefore, particular attention must be paid when selecting an appropriate dmax to avoid significant mesh distortion, which can result in inaccurate results. In this study, the dmax was varied from 5 to 20 mm.

#### *Optimum shape and 3-D enclosure design*

After determining the optimum enclosure shape in COMSOL Multiphysics, the shape was imported into SOLIDWORKS, where a 3-D enclosure design was modelled. The enclosure was 3-D printed to be tested on the actuator using hotwire anemometry and a microphone to evaluate its flow and acoustic performance, respectively,

## IV. Results and Discussion

Two models, Turbulence SST and Turbulence SA, were investigated to determine the most suitable turbulence model for the study. Their results and computational time on each mesh size were compared (Figure 7).

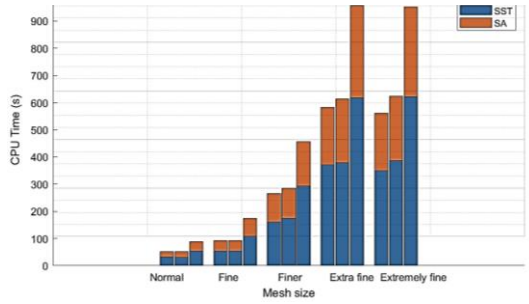


Figure 7. CPU time of Turbulence SST and Turbulence SA across mesh sizes for the three designs.

In all three designs, the Turbulence SA's computational cost was less than that of the Turbulence SST by up to 50%, which can be attributed to the one-equation formulation nature of the SA model. For both turbulence models, a decrease in mesh size results in an increase in computer run time.

The pressure and velocity conditions at the inlet and outlet of the enclosure and the total viscous dissipation were recorded in each case. The pressure drop ΔP obtained from both models at the different mesh sizes was calculated for all three designs. The maximum percentage difference in pressure drop was 0.27% for Design 1, 0.056% for Design 2, and 0.39% for Design 3. The slight difference in pressure drop values indicated that the turbulence models predicted the flow behaviour similarly. From the results, the Turbulence SA model was selected as a study model for this research because of its efficiency while producing results similar to Turbulence SST.

#### *Mesh Sensitivity Analysis*

Five physics-controlled meshes were studied, and conclusions were drawn on (i) the influence of mesh size on accuracy and (ii) the computer run time variation with mesh size. The computational accuracy was determined by investigating the residual pressure at the enclosure outlet (enclosure secondary orifice). The outlet boundary condition was set to 0 Pa static/gauge pressure, as the tested actuator operates under atmospheric pressure. Pressure values at the outlet after simulation had to be as close to 0 Pa as possible to indicate full convergence and accuracy. Table IV.1 shows the pressure values at the outlet for the three designs across the different mesh sizes.

Table IV.1. Residual pressure generated at each mesh size.

| | **Residual Pressure $P_{out}$ (Pa)** | | |
|---|---|---|---|
| **Mesh size** | **Design 1** | **Design 2** | **Design 3** |
| **Normal** | 1.434 | 8.829 | 29.38 |
| **Fine** | 1.035 | 4.614 | 13.204 |
| **Finer** | 0.593 | 2.290 | 6.527 |
| **Extra fine** | 0.504 | 2.150 | 5.714 |
| **Extremely fine** | 0.504 | 2.150 | 5.714 |

The table shows that the residual pressure decreased as mesh size decreased, indicating improvement in convergence and accuracy for finer meshes. Design 1 has the most accurate results, showing that the design is easier to solve with less complex meshes.

#### *Adaptive Mesh Refinement*

Two adaptive meshes were generated in COMSOL for Design 1, three for Design 2, and four for Design 3. The number of degrees of freedom solved for, the residual pressure, and the computation time were recorded for each design.

Table IV.2. Adaptive Mesh Refinement Results for Design 1.

| **Mesh** | **Degrees of freedom solved** | **Residual Pressure (Pa)** | **CPU Time (s)** |
|---|---|---|---|
| **Extremely fine** | 81974 | 0.504 | 213 |
| **Refinement 1** | 118012 | 0.0654 | 203 |
| **Refinement 2** | 266204 | -0.0028 | 429 |

Table IV.2 shows a reduction in residual pressure of 87 % between the extremely fine mesh and the first refined mesh for a similar computation time. For Design 2 and 3, a reduction in residual pressure of 89 % and 86 %, respectively, is observed on the first refined mesh. The results obtained validate the importance of mesh refinement for accuracy improvement.

*Efficiency and Pressure Drop Comparison*

Table IV.3. Comparison between pressure drop and efficiency for the 3 designs.

| Design | Efficiency | Pressure Drop ΔP (Pa) | CPU Time (s) |
|---|---|---|---|
| **1** | 0.905 | 115.7 | 203 |
| **2** | 0.931 | 111.06 | 1079 |
| **3** | 0.895 | 115.3 | 1176 |

Designs 1 and 2 were the most efficient. Design 3 had a slightly lower pressure drop than Design 1, but comparing the computation times, Design 1 was best because of its cost-effectiveness. Therefore, the best designs were Design 1 and 2.

*Parameter Sensitivity Analysis and Geometric Optimization*

Both Parametric Sweep and gradient-free optimization were performed using a stretch factor k that elongated the enclosure from 130 mm to 156 mm. 156 mm was selected as the maximum to accomplish the objective of a compact enclosure.

Table IV.4. Results from the Geometric Optimization of Design 1.

| Algorithm | Objective ΔP (Pa) | Optimum stretch *k* | Iter-ations | CPU Time (s) |
|---|---|---|---|---|
| **BOBYQA** | 114.42 | 1.063 | 20 | 5104 |
| **COBYLA** | 114.44 | 1.05 | 8 | 3807 |
| **Nelder-Mead** | 114.44 | 1.05 | 13 | 5528 |

The Parametric Sweep conducted on Design 1 provided the optimum stretch factor $k = 1.05$ ($L_{encl} = 136.5$ mm). Results from Design 2 obtained the optimum stretch factor of 1.1 ($L_{encl} = 143$mm) with a minimum pressure drop of 110.9 Pa.

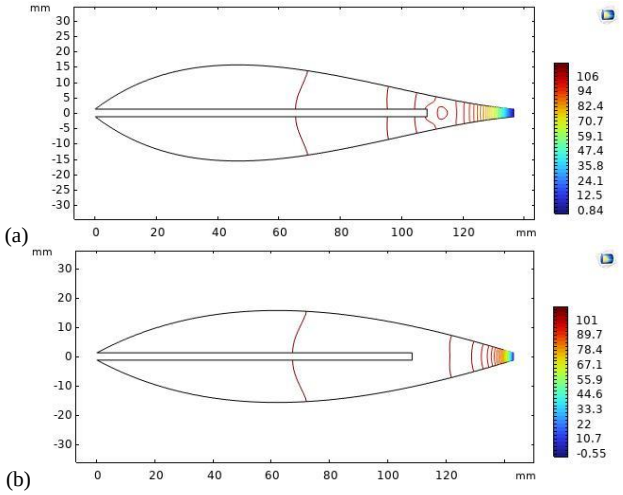


Figure 8. Plot of pressure contours of Design (a)1 and (b) 2 with optimum length.

Figure 8 shows pressure contour plots of the enclosure lengths obtained via geometric optimization or parameter sensitivity analysis. The separation bubble at the end of the actuator indicates a region of recirculated flow.

*Shape Optimization*

Shape optimization was performed with varying dmax from 5 to 20 mm. Design 2 did not improve with shape optimization, concluding that its minimum pressure drop of 110.9 Pa is its best. Only Design 1 was simulated, and the results of Design 1 with IPOPT are shown in Table IV.5.

Table IV.5. Results of varying dmax in shape optimization.

| $d_{max}$ (mm) | Pressure Drop Δ*P* (Pa) |
|---|---|
| **5** | 110.36 |
| **10** | 108.7 |
| **15** | 108.71 |
| **20** | 108.77 |

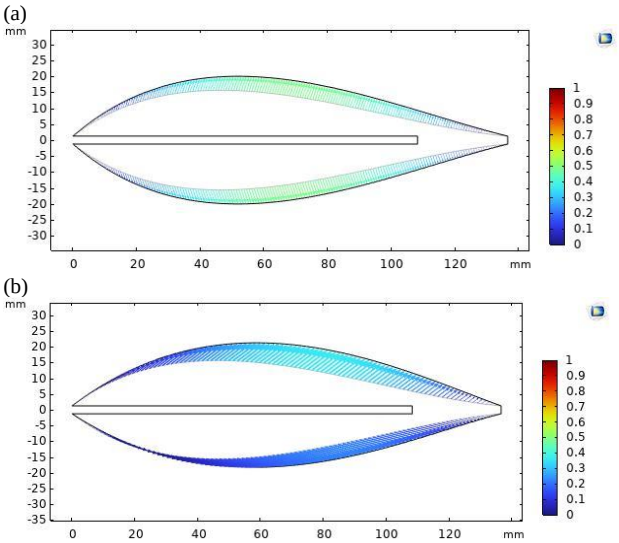


Figure 9. Shape optimization graphs for (a) best, and (b) least effective design.

Figure 9(b) is asymmetric and gives a higher pressure drop. This is due to the high $d_{max}$, which could have resulted in poor mesh generation (over-deformation of the mesh).

The best shape was obtained at $d_{max} = 10$mm, achieving a pressure drop of 108.7 Pa. Figure 10 shows the associated pressure contours.

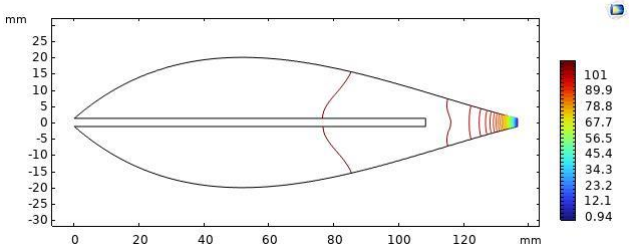


Figure 10. Plot of pressure contours of the optimized shape.

The shape was imported into SOLIDWORKS and used to design the 3-D enclosure (Figure 11).

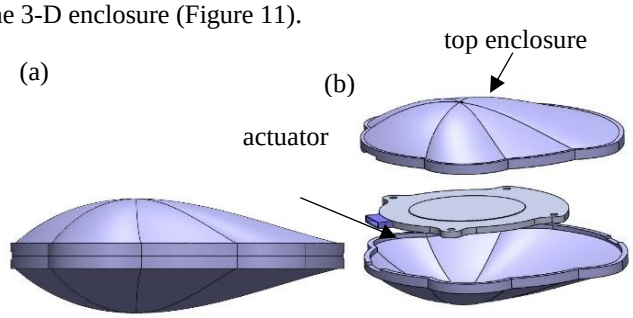


Figure 11. The optimized enclosure in (a) assembled view (b) exploded view.

## V. CONCLUSION

The main objective of the study was to determine the optimum shape of a synthetic jet actuator enclosure through various processes leading to shape optimization. The hypothesis was that a streamlined enclosure improves the overall performance of an SJA; therefore, the enclosure was designed and optimized to minimize losses in the viscous flow inside the enclosure, thereby maximizing the enclosure efficiency.

The preliminary study to determine the best turbulence model showed that the Turbulence SA was more efficient, operating at almost half the time of the Turbulence SST. The mesh refinement study showed that smaller-sized meshes produced more accurate results. Furthermore, adaptive mesh refinement gives more convergent results. It is thus important to analyze the generated meshes and determine a mesh that accomplishes the accuracy needed while minimizing the computational costs.

Parameter sensitivity analysis showed how changes in geometric parameters influenced flow performance. In this study, the enclosure was stretched from 130 mm to 156 mm, and the optimum enclosure lengths for Design 1 and 2 were 136.5 mm and 143 mm, respectively. Shape optimization using the SNOPT and IPOPT at various $d_{max}$ produced the highest efficiency of 0.96 and minimum pressure drop of 108.7 Pa for Design 1. Higher values of $d_{max}$ distorted the mesh, resulting in inaccurate results.

The 3-D-designed enclosure was 3D printed and set for experimental testing. For future works, the enclosure will be tested on an actuator, and the centerline jet velocity and sound pressure levels will be measured using the hot wire anemometer and microphone, respectively. The experimental setup is shown in Figure 12.

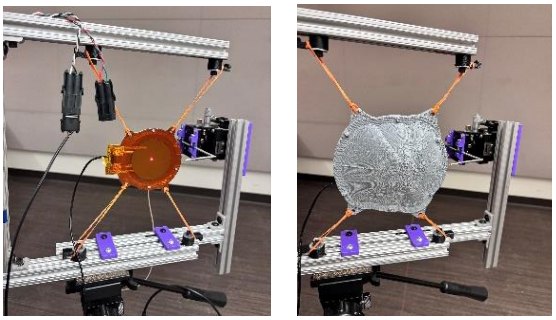

Figure 12. Experimental setup with the hot wire and microphone for the (a) actuator only and (b) actuator and enclosure.


## ACKNOWLEDGMENT

The first author would like to acknowledge the financial support of the Natural Sciences and Engineering Research Council of Canada (NSERC) and the McCall MacBain Scholarships at McGill Finalist Award.


## REFERENCES


[1] M. Ja'fari, F. J. Shojae, and A. J. Jaworski, "Synthetic Jet Actuators: Overview and Applications," *International Journal of Thermofluids*, vol. 20, p. 100438, Nov. 2023. doi:10.1016/j.ijft.2023.100438

[2] Z. Luo, Z. Xia, and B. Liu, "An adjustable synthetic jet by a novel PZT-driven actuator with a slide block," *Journal of Physics: Conference Series*, vol. 34, pp. 487–492, Apr. 2006. doi:10.1088/1742-6596/34/1/080.

[3] E. Smyk, P. Gil, R. Gałek, and Ł. Przeszłowski, "Acoustic and flow aspects of novel Synthetic Jet Actuator," *Actuators*, vol. 9, no. 4, p. 100, Oct. 2020. doi:10.3390/act9040100.

[4] C. Y. Y. Lee, M. L. Woyciekoski, and J. B. Copetti, "Experimental study of synthetic jets with rectangular orifice for electronic cooling," *Experimental Thermal and Fluid Science*, vol. 78, pp. 242–248, Nov. 2016. doi:10.1016/j.expthermflusci.2016.06.007.

[5] F. Xu *et al.*, "The optimization for the backward-facing step flow control with synthetic jet based on experiment," *Experimental Thermal and Fluid Science*, vol. 64, pp. 94–107, Jun. 2015. doi:10.1016/j.expthermflusci.2015.02.014

[6] M. G. Butler, A. Ekmekci, and P. E. Sullivan, "Multiphysics modeling of a synthetic jet actuator in Operation," *Actuators*, vol. 13, no. 2, p. 60, Feb. 2024. doi:10.3390/act13020060

[7] Z. He, L. Mongeau, R. Taduri, and D. Menicovich, "Feedforward harmonic suppression for noise control of piezoelectrically driven synthetic jet actuators," *SAE Technical Paper Series*, May 2023. doi:10.4271/2023-01-1042

[8] M. Jabbal and J. Jeyalingam, "Towards the noise reduction of piezoelectrical-driven synthetic jet actuators," *Sensors and Actuators A: Physical*, vol. 266, pp. 273–284, Oct. 2017. doi:10.1016/j.sna.2017.09.036

[9] S. Wang *et al.*, "Acoustical analysis of sound generated by synthetic jet actuators," *INTER-NOISE and NOISE-CON Congress and Conference Proceedings*, vol. 263, no. 2, pp. 4823–4831, Aug. 2021. doi:10.3397/in-2021-2851

[10] E. Ermakova and M. Rynkovskaya, "Using shape optimization settings in COMSOL multiphysics for efficient structural design of Shells," *Lecture Notes in Civil Engineering*, pp. 427–435, Oct. 2023. doi:10.1007/978-3-031-44328-2_44

[11] D. C. Wilcox, *Turbulence Modelling for CFD*. La Canada, California: DCW Industries, 1994

[12] P. SPALART and S. ALLMARAS, "A one-equation turbulence model for aerodynamic flows," *30th Aerospace Sciences Meeting and Exhibit*, Jan. 1992. doi:10.2514/6.1992-439

[13] F. R. Menter, "Two-equation eddy-viscosity turbulence models for engineering applications," *AIAA Journal*, vol. 32, no. 8, pp. 1598–1605, Aug. 1994. doi:10.2514/3.12149

[14] J. Tu, G.-H. Yeoh, and C. Liu, "CFD Mesh Generation: A practical guideline," *Computational Fluid Dynamics*, pp. 125–154, 2018. doi:10.1016/b978-0-08-101127-0.00004-0

[15] R. W. Fox, A. T. McDonald, and P. J. Pritchard, *Introduction to Fluid Mechanics*, 6th ed. Hoboken, New Jersey: John Wiley & Sons, Inc, 2004

[16] P. J. Pritchard and J. C. Leylegian, *Fox and McDonald's Introduction to Fluid Mechanics*, 8th ed. Hoboken, NJ: John Wiley & Sons, Inc, 2011.

[17] Optimization Module User's Guide. COMSOL Version 6.3. 1998-2024. Available [online]

[18] Leyffer, S., and Mahajan, A, *Nonlinear Constrained Optimization: Methods and Software; Argonne National Laboratory*: Lemont, IL, USA, 2010.